The Astrophysical Journal Letters, 914:L29 (7pp), 2021 June 20 https://doi.org/10.3847/2041-8213/ac0636

Discovery of a Radio Halo (and Relic) in a $M_{500} < 2 \times 10^{14}\ M_{\odot}$ Cluster

A. Botteon[1], R. Cassano[2], R. J. van Weeren[1], T. W. Shimwell[1,3], A. Bonafede[2,4], M. Brüggen[5], G. Brunetti[2], V. Cuciti[5], D. Dallacasa[2,4], F. de Gasperin[5,2], G. Di Gennaro[1], F. Gastaldello[6], D. N. Hoang[5], M. Rossetti[6], and H. J. A. Röttgering[1]

[1] Leiden Observatory, Leiden University, P.O. Box 9513, 2300 RA Leiden, The Netherlands; botteon@strw.leidenuniv.nl
[2] INAF—IRA, via P. Gobetti 101, I-40129 Bologna, Italy
[3] ASTRON, the Netherlands Institute for Radio Astronomy, Postbus 2, 7990 AA Dwingeloo, The Netherlands
[4] Dipartimento di Fisica e Astronomia, Università di Bologna, via P. Gobetti 93/2, I-40129 Bologna, Italy
[5] University of Hamburg, Hamburger Sternwarte, Gojenbergsweg 112, D-21029 Hamburg, Germany
[6] INAF—IASF Milano, via A. Corti 12, I-20133 Milano, Italy
Received 2021 May 8; revised 2021 May 25; accepted 2021 May 28; published 2021 June 17

Abstract

Radio halos are diffuse synchrotron sources observed in dynamically unrelaxed galaxy clusters. Current observations and models suggest that halos trace turbulent regions in the intracluster medium where mildly relativistic particles are reaccelerated during cluster mergers. Due to the higher luminosities and detection rates with increasing cluster mass, radio halos have been mainly observed in massive systems ($M_{500} \gtrsim 5 \times 10^{14}\ M_{\odot}$). Here, we report the discovery of a radio halo with a largest linear scale of $\simeq$750 kpc in PSZ2G145.92-12.53 ($z = 0.03$) using LOw Frequency ARray (LOFAR) observations at 120–168 MHz. With a mass of $M_{500} = (1.9 \pm 0.2) \times 10^{14}\ M_{\odot}$ and a radio power at 150 MHz of $P_{150} = (3.5 \pm 0.7) \times 10^{23}$ W Hz^{-1}, this is the least powerful radio halo in the least massive cluster discovered to date. Additionally, we discover a radio relic with a mildly convex morphology at $\sim$1.7 Mpc from the cluster center. Our results demonstrate that LOFAR has the potential to detect radio halos even in low-mass clusters, where the expectation to form them is very low ($\sim$5%) based on turbulent reacceleration models. Together with the observation of large samples of clusters, this opens the possibility to constrain the low end of the power–mass relation of radio halos.

Unified Astronomy Thesaurus concepts: Galaxy clusters (584); Intracluster medium (858); Extragalactic radio sources (508); Radio astronomy (1338); Radio interferometry (1346); Extended radiation sources (504); Non-thermal radiation sources (1119)

1. Introduction

Radio halos are extended synchrotron sources with steep spectra ($\alpha > 1$, with $S_{\nu} \propto \nu^{-\alpha}$ where S_{ν} is the flux density at frequency ν and α is the spectral index) that are often observed in massive merging galaxy clusters (e.g., van Weeren et al. 2019 for a review). Their emission generally follows the distribution of the thermal gas of the intracluster medium (ICM), and occupies the central volume of the cluster. Nowadays, turbulent reacceleration is thought to be the main mechanism responsible for generating radio halos (e.g., Brunetti & Jones 2014 for a review). In this scenario, relativistic electrons in halos are reenergized due to the interaction with MHD turbulence that has been injected in the ICM during cluster collisions. The competition between energy losses and acceleration of particles (that is connected to the energetics of the merger) results in a gradual steepening of the halo spectrum at higher frequencies (e.g., Cassano & Brunetti 2005). This implies that, especially when observed at GHz frequencies, they should preferentially be found in massive objects undergoing energetic merging events and be rarer in less massive merging systems (Cassano et al. 2006).

The radio halo power is found to increase with the cluster mass and/or X-ray luminosity (e.g., Feretti et al. 2012; van Weeren et al. 2019), implying that it is more challenging to observe radio halos in lower-mass systems. For this reason, Giant Metrewave Radio Telescope (GMRT) and Very Large Array (VLA) observations have been focused mainly on massive ($M_{500} \gtrsim 5 \times 10^{14}\ M_{\odot}$) or X-ray bright ($L_X \gtrsim 5 \times 10^{44}$ erg s^{-1}), nearby ($z \lesssim 0.4$) clusters (Venturi et al. 2007; Giovannini et al. 2009; Cassano et al. 2013; Kale et al. 2013, 2015; Cuciti et al. 2015, 2021a, 2021b). However, one major expectation of the reacceleration scenario is that the occurrence of radio halos should be higher at low frequencies, where radio halos also generated during less energetic events, i.e., in low-mass clusters or in minor mergers, should be visible (Cassano et al. 2006, 2010). The LOw Frequency ARray (LOFAR) is enabling highly sensitive observations at $<$200 MHz, which allow us to probe the population of radio halos in the relatively poorly explored regimes of high-z (Cassano et al. 2019; Di Gennaro et al. 2021) and low-mass systems (Botteon et al. 2019; Hoang et al. 2019, 2021; Osinga et al. 2021).

In this Letter, we report on the discovery of a radio halo (and relic) in PSZ2G145.92-12.53. This cluster belongs to the Clusters in the Zone of Avoidance sample (CIZA; Ebeling et al. 2002) and to the second Planck Sunyaev–Zel'dovich (SZ) catalog (PSZ2; Planck Collaboration et al. 2016), is located at $z = 0.03$ (Ebeling et al. 2002), and has a SZ-derived mass of $M_{500} = (1.9 \pm 0.2) \times 10^{14}\ M_{\odot}$, consistent with that reported by PSZ1 ($\simeq 1.8 \times 10^{14}\ M_{\odot}$; Planck Collaboration et al. 2014) and in the Meta-Catalogue of X-ray detected Clusters of galaxies ($\simeq 1.9 \times 10^{14}\ M_{\odot}$; Piffaretti et al. 2011). Owing to its low-mass and (radio) power, we nickname it the Ant Cluster. Throughout this work, we adopt a ΛCDM cosmology with $\Omega_{\Lambda} = 0.7$, $\Omega_{\rm m} = 0.3$, and $H_0 = 70$ km s^{-1} Mpc^{-1}. At $z = 0.03$, this corresponds to a luminosity distance of $D_{\rm L} = 131.4$ Mpc and to an angular scale of 36.1 kpc arcmin^{-1}.

2. Data Reduction

2.1. LOFAR

The Ant Cluster is located $\sim 0.^{\circ}95$ from the center of the LOFAR Two-meter Sky Survey (LoTSS; Shimwell et al. 2017, 2019) pointing P044+44, which was observed for 8 hr on 2018 December 14. Observations were carried out in `HBA_DUAL_INNER` mode adopting a bandwidth of 48 MHz (120–168 MHz band), centered at 144 MHz. Preliminary data processing was carried out by the LOFAR Surveys Key Science Project team adopting the same pipelines used to correct for direction-independent and direction-dependent effects across the entire field of view (FoV) of LoTSS observations (van Weeren et al. 2016; de Gasperin et al. 2019; Shimwell et al. 2019; Tasse et al. 2021). In particular, direction-dependent calibration is performed with `ddf-pipeline`,[7] which also delivers images of the entire LOFAR FoV at $6''$ and $20''$ resolution. We then obtained images suitable for our study following two approaches.

First, we created a very low resolution source-subtracted image of an FoV of $1.^{\circ}6 \times 2.^{\circ}1$ centered on the Ant Cluster. In this case, we used the $20''$ resolution model of P044+44 obtained from `ddf-pipeline` to subtract sources in the whole FoV, taking care to exclude any clean components associated with the cluster. The *uv* data were then reimaged at $180'' \times 180''$ resolution (corresponding to $\simeq$106 kpc $\times$ 106 kpc at the cluster redshift) and corrected for the primary beam response. This image was obtained only for visualization purposes, and was not used further in the analysis. LoTSS images at $6''$ and $20''$ of the same FoV without discrete sources subtracted are shown in the Appendix.

Second, we refined the calibration toward two regions of interest (halo and relic regions) following the "extraction and recalibration" method described in van Weeren et al. (2021). Briefly, this method consists of removing all sources outside a region containing the target from the *uv* data, phase shifting to the center of the region while averaging the data to speed up further processing, correcting for the LOFAR primary beam response, and performing phase and amplitude self-calibration loops in the extracted region. The improved calibration provided by this approach allows us to study better the cluster diffuse radio emission and to measure its flux density. For this reason, all the flux densities reported in this Letter were evaluated using these data sets. Each of the reprocessed regions was reimaged at two different resolutions, with and without discrete sources (modeled and subtracted using the improved data sets).

Our final LOFAR images are visualized in Figure 1 and their noise and resolution are summarized in Table 1. All images were produced with WSCLEAN v2.10 (Offringa et al. 2014) adopting an inner *uv* cut of 80λ (corresponding to an angular scale of $43'$) to reduce sensitivity to extended Galactic emission. Uncertainties on the LOFAR integrated flux densities are dominated by errors in the absolute flux scale, which is conservatively set to 20%, in line with LoTSS measurements (Shimwell et al. 2019). The flux scale of the LOFAR images was aligned adopting the NRAO VLA Sky Survey (NVSS; Condon et al. 1998) derived multiplicative correction factor of 0.876 on LOFAR data, following Hardcastle et al. (2021).

[7] https://github.com/mhardcastle/ddf-pipeline

2.2. ROSAT and XMM-Newton

ROSAT count images in the energy band 0.1–2.4 keV in the direction of the Ant Cluster were retrieved together with the corresponding background and exposure maps from the ROSAT All-Sky Survey (RASS; Voges et al. 1999) data archive.[8] These data were combined to produce the count rate image smoothed with a Gaussian kernel with $\sigma = 3$ pixels (1 pixel $= 45''$) that is shown in Figure 1.

From the XMM-Newton Science Archive,[9] we retrieved a pointed observation of the cluster (ObsID: 0744100301, 14 ks). We made use of the XMM-Newton Scientific Analysis System (SAS v16.1.0) to create clean event files using the tasks `mos-filter` and `pn-filter`. The MOS1, MOS2, and pn data were then combined to produce a 0.5−2.0 keV count rate image that was smoothed with a Gaussian kernel with $\sigma = 3$ pixels (1 pixel $= 2.''5$). The resulting image, which covers only the central region of the cluster, is shown in Figure 2.

3. Results

In the left panel of Figure 1, we show a radio/X-ray (LoTSS/RASS) overlay of a large FoV centered on the Ant Cluster. The thermal emission of the ICM (blue) is elongated in the N–S direction, suggesting that the cluster is dynamically unrelaxed. The LOFAR discrete source-subtracted image (red) highlights the presence of diffuse emission at the center of the cluster that is connected to a brighter and elongated structure to the W, which we term the Rim. At $\sim$1.7 Mpc N from the cluster center, a source extended in the the E–W direction is also detected. Its surface brightness drops rapidly to the N, while it declines more slowly toward the cluster. The zoom-in images of these two regions of interest are depicted in the right panels of Figure 1.

Due to the morphology, location in the cluster, and largest linear size of $\simeq$750 kpc, we classify the central diffuse emission as a radio halo. This classification is supported by the morphological similarity between the X-ray and radio emission, which can be better observed in Figure 2 where we overlay the LOFAR contours onto the XMM-Newton image of the cluster center. The absence of a compact and peaked X-ray core and the elongated X-ray morphology revealed in the higher-resolution XMM-Newton data is indicative of a merging system, confirming the impression from the RASS image. The hypothesis that the radio emission in the Ant Cluster is tracing a mini-halo (i.e., another kind of diffuse emission that can be found at the center of galaxy clusters) is rejected due to its large linear size, the lack of a powerful radio galaxy at its center, and the absence of a cool core in the system. The Rim, roughly separated from the halo by the dashed line in Figure 2, is located in a region of lower gas density, in a direction where the X-ray emission from the ICM has a protuberance. The total flux density of the diffuse emission measured within the 2.5σ low-resolution level contour is 253 ± 51 mJy, divided into $\simeq$155 mJy for the halo and $\simeq$98 mJy for the Rim. We also measure the flux density of the radio halo by fitting its surface brightness profile in 2D using the Halo-Flux Density CAlculator[10] (HALO-FDCA; Boxelaar et al. 2021) and adopting an exponential profile (see also Murgia et al. 2009). Due to the elongation of the halo, we assumed an elliptical model, which

[8] https://heasarc.gsfc.nasa.gov/docs/rosat/rass.html
[9] http://nxsa.esac.esa.int/nxsa-web/
[10] https://github.com/JortBox/Halo-FDCA

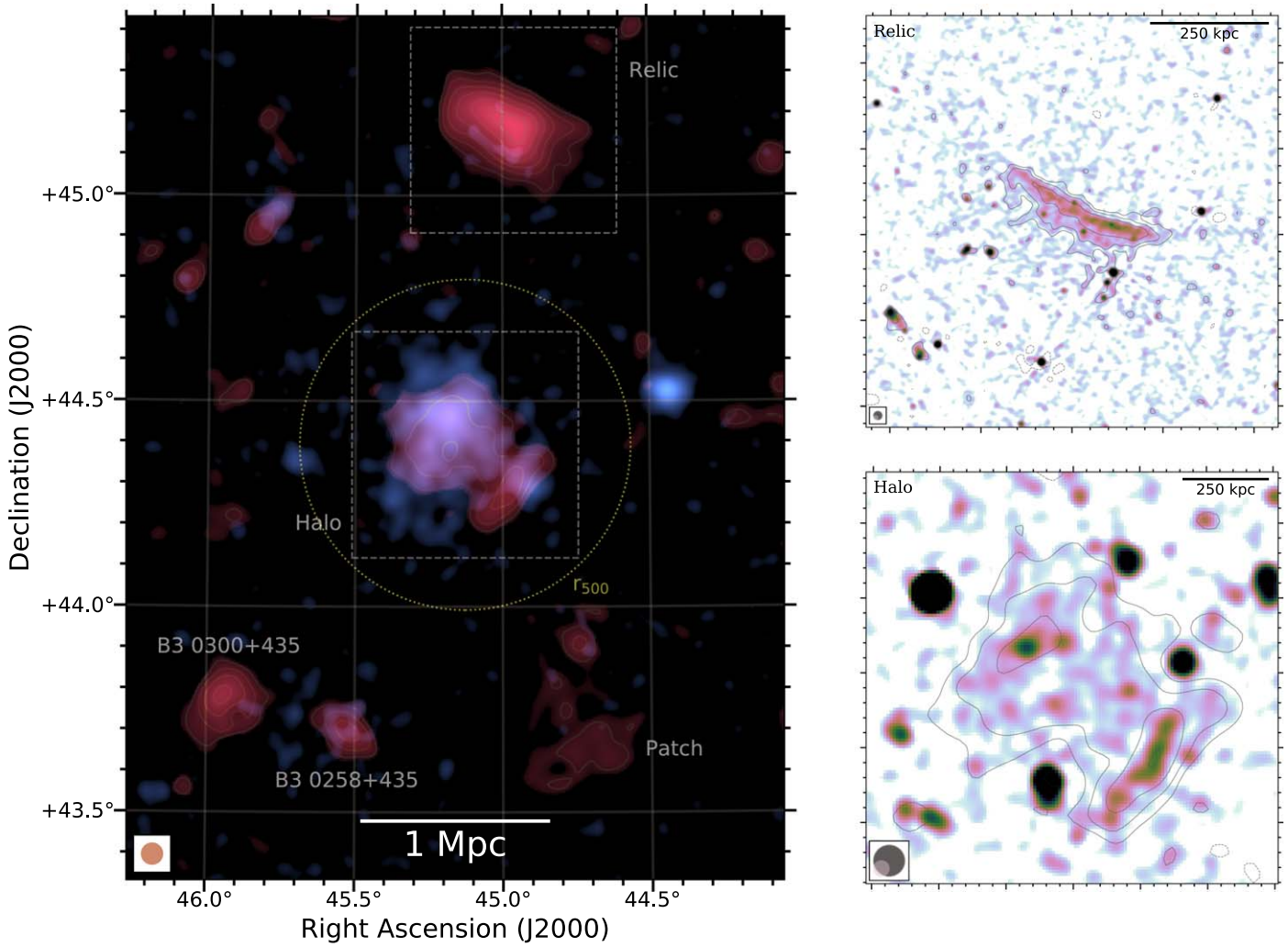

Figure 1. Left panel: composite radio (LOFAR 120−168 MHz, red) + X-ray (ROSAT 0.1–2.4 keV, blue) image of a $1.^{\circ}6 \times 2.^{\circ}1$ field centered on the Ant Cluster. The LOFAR image has a resolution of 180″ and was obtained after subtracting discrete sources in the *uv* plane. The dashed boxes mark the regions where we improved the calibration of LoTSS data. Right panels: zoom-in of the (reprocessed) relic and halo regions. Colors indicate the images at 15″ and 75″ resolution for the relic and halo, respectively. Contours show the discrete source-subtracted emission from images with double beamwidth. Contours are spaced by a factor of 2 starting from 2.5σ. The -2.5σ contour is reported with dashed lines. The beam of the radio images is shown in the bottom left corners. The noise level and resolution are listed in Table 1.

Table 1
Properties of the LOFAR Images Shown in Figure 1

Field	Resolution (″ × ″)	Noise (μJy beam^{-1})	Discrete Sources
Full	180 × 180	1050	subtracted
Relic (colors)	15 × 15	307	present
Relic (contours)	30 × 30	438	subtracted
Halo (colors)	75 × 75	596	present
Halo (contours)	150 × 150	876	subtracted

has six free parameters: the coordinates of the center (x_0 and y_0), the central brightness (I_0), two *e*-folding radii (r_1 and r_2), and a rotation angle (ϕ). The Rim region was masked out during the fit. The relevant best-fit physical quantities of the model are $I_0 = 0.62 \pm 0.04$ μJy arcsec^{-2}, $r_1 = 166 \pm 12$ kpc, and $r_2 = 122 \pm 9$ kpc, and the model appears to provide an accurate description of the data (χ^2/dof = 376.07/377). The flux density at 150 MHz obtained by integrating this model up to three times the *e*-folding radii (as suggested by Murgia et al. 2009) and assuming a spectral index value of $\alpha = 1.5 \pm 0.3$ (which covers the typical range observed for radio halo spectra; e.g., Feretti et al. 2012; van Weeren et al. 2019) is $S_{150} = 167 \pm 35$ mJy, consistent within uncertainties with that measured in the 2.5σ contour. Hereafter, we adopt this flux density value for the radio halo, which leads to a radio power at 150 MHz of $P_{150} = (3.5 \pm 0.7) \times 10^{23}$ W Hz^{-1}.

We classify the peripheral emission in the cluster N outskirts as a radio relic. Radio relics are diffuse sources observed in merging clusters that trace synchrotron emitting electrons (re) accelerated at merger shocks. The source position in the system, its major axis elongated perpendicularly with respect to the main elongation of the ICM thermal emission (which generally indicates the merger axis), its brightness distribution declining toward the cluster center, and the absence of a clear optical counterpart support this classification. Its flux density (measured within the 2.5σ low-resolution contour) is 275 ± 55 mJy, corresponding to a power of $(5.7 \pm 1.1) \times 10^{23}$ W Hz^{-1}. We note that the relic can be also observed with low significance in the NVSS at 1.4 GHz; however, the limited sensitivity and poor resolution of NVSS does not allow us to provide a meaningful constraint on its spectral index.

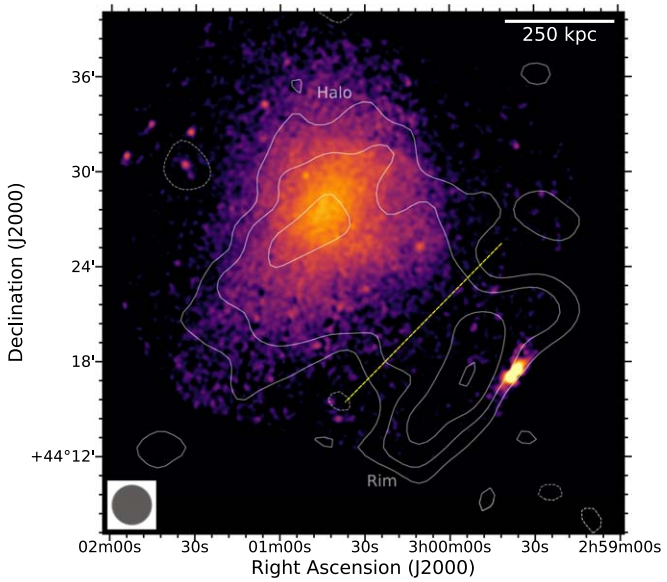

Figure 2. XMM-Newton image in the 0.5–2.0 keV with overlaid the LOFAR source-subtracted contours at 150″ resolution of Figure 1. The dashed yellow line separates the halo and Rim regions.

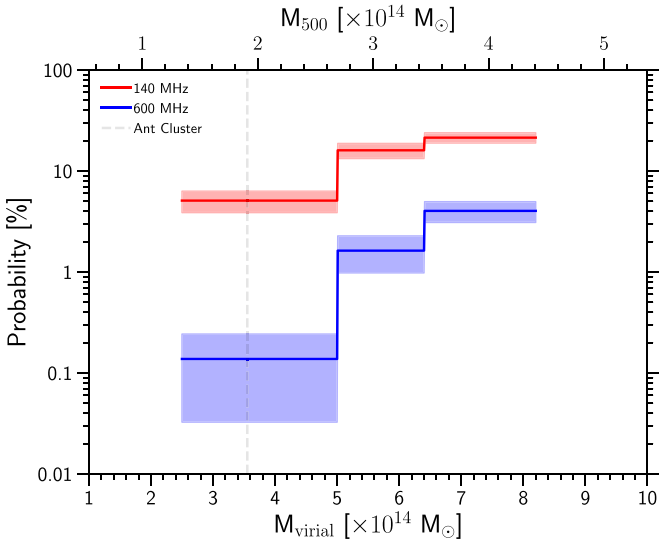

Figure 3. Probability of forming radio halos with $\nu_s \gtrsim 140$ MHz and $\nu_s \gtrsim 600$ MHz (red and blue lines, respectively) as a function of the cluster mass in the redshift range $z = 0$–0.1. A magnetic field of $B = 2\,\mu$G is assumed. The shadowed regions represent the 1σ uncertainty derived through Monte Carlo calculations. The dashed vertical line indicates the mass of the Ant Cluster.

Finally, we note the presence of three other prominent sources in the large FoV image of the Ant Cluster (marked Figure 1). While the emissions labeled B3 0300+435 and B3 0258+435 (Ficarra et al. 1985) may well be residuals left over by the subtraction of these two bright and extended sources, we exclude that the Patch is an artifact because of the lack of sources in that region in the LoTSS 6″ resolution image of P044+44 (see the Appendix). This emission arises only at very low resolution ($\gtrsim$150″), is detected just above the 2σ level, and possibly shows an elongation toward the cluster center.

4. Discussion

4.1. Radio Halo

The Ant Cluster is the least massive cluster known to host a radio halo, allowing us to probe nonthermal phenomena in the low-mass end of the cluster mass function. So far there are only a handful of central, extended, diffuse sources detected in clusters with mass $M_{500} \lesssim 4 \times 10^{14}\ M_\odot$ (e.g., A3562, Venturi et al. 2000, 2003; Giacintucci et al. 2005; A2061, Rudnick & Lemmerman 2009; PSZ1G018.75+23.57, Bernardi et al. 2016; A2146, Hlavacek-Larrondo et al. 2018; Hoang et al. 2019; RXCJ1825.3+3026, Botteon et al. 2019; A1775, Botteon et al. 2021) and no radio halos have been claimed below $M_{500} < 2 \times 10^{14}\ M_\odot$. LOFAR is increasing the number of radio halos observed in low-mass systems thanks to the wide area covered by LoTSS-DR2 (T. W. Shimwell et al. 2021, in preparation) and the Deep Fields observations (Osinga et al. 2021). Currently, the Ant Cluster is the clearest halo in the lowest-mass PSZ2 cluster that we have found after searching LoTSS images spanning ∼35% of the northern sky.

In the context of turbulent reacceleration, radio halos originate during cluster–cluster mergers where a small fraction of gravitational energy is dissipated by large-scale motions into particle acceleration on much smaller scales (e.g., Brunetti & Jones 2014). The energetics of the merger depends on the mass of the colliding clusters (e.g., Sarazin 2002), thus the formation of observable levels of synchrotron emitting electrons is favored in massive systems. This is reflected in the observed steep correlation between radio halo power and cluster mass (e.g., Cassano et al. 2013) and in the observed increase of the occurrence of radio halos with the cluster mass (e.g., Cuciti et al. 2021b). Both these observational facts are probed for massive clusters ($M_{500} \gtrsim 5 \times 10^{14}\ M_\odot$) and at GHz frequencies.

According to reacceleration models, the occurrence of radio halos should increase at lower frequency especially for less massive systems due to the presence of ultra-steep-spectrum radio halos (e.g., Cassano et al. 2006, 2010). As spectral steepening in radio halos makes it difficult to detect them at frequencies higher than the frequency ν_s at which the steepening becomes severe, one can assume that a radio halo can be successfully detected at a given frequency ν_0 only when $\nu_s > \nu_0$. To derive the expected probability to form a radio halo with a given ν_s we use the statistical model developed in Cassano & Brunetti (2005; see also Cassano et al. 2006, 2010), which is based on a Monte Carlo approach to describe the merger history of galaxy clusters, to calculate the generation of turbulence, the particle acceleration, and the synchrotron spectrum during the cluster lifetime. In Figure 3 we show the probability of forming a radio halo as a function of the cluster mass, in the redshift range $z = 0$–0.1, with a steepening frequency $\nu_s \gtrsim 140$ MHz and $\nu_s \gtrsim 600$ MHz. We find that, for a cluster with a mass similar to that of the Ant Cluster, the probability of forming a radio halo with steepening frequency $\nu_s \gtrsim 140$ MHz is ∼5% (red line), while it decreases down to a few per thousand for $\nu_s \gtrsim 600$ MHz (blue line), with a clear dependence on cluster mass. The large difference expected between the two fractions implies that a large number of these halos should have very steep radio spectra. The calculations assume a mean rms magnetic field average over the radio halo volume of $B = 2\,\mu$G. Decreasing the magnetic field to $B = 1\,\mu$G has only a small impact in the formation probability at 140 MHz (well within the reported uncertainties), while a more important decrement is expected at 600 MHz. These

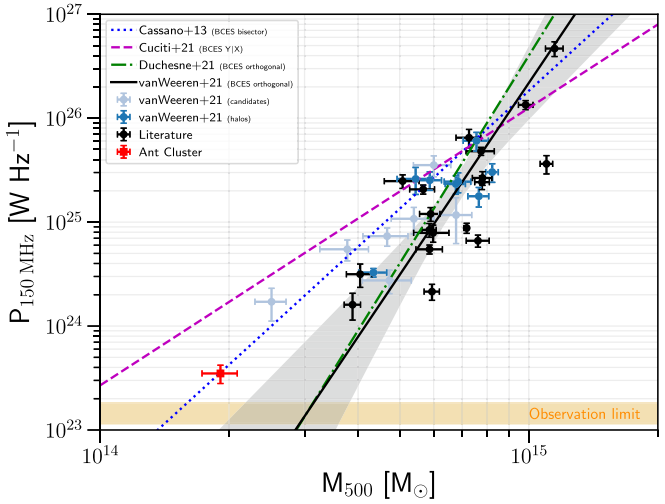

Figure 4. The position of the Ant Cluster in the P_{150}–M_{500} relation of van Weeren et al. (2021). The reference scaling relations reported by Cassano et al. (2013), Cuciti et al. (2021b), and Duchesne et al. (2021), rescaled to 150 MHz adopting $\alpha = 1.3$, are also shown. The orange horizontal region marks the detection limit for our LOFAR 180″ image.

B values have been chosen to be in line with the magnetic field strengths at $\sim\mu$G levels observed in galaxy clusters (e.g., Govoni & Feretti 2004 for a review).

In Figure 4 we plot the position of the Ant Cluster in the P_{150}–M_{500} relation from van Weeren et al. (2021). The Ant Cluster is the least powerful radio halo observed to date, and lies in a region where we need to extrapolate the known relations. Its position on the diagram shows that with LOFAR we are entering an unexplored regime of cluster mass. Only with the analysis of large statistical samples of clusters, taking into account possible selection effects (e.g., completeness in mass) and observational biases (e.g., sensitivity of radio observations), will it be possible to firmly constrain the slope of the P_{150}–M_{500} relation.

Future X-ray and radio surveys performed with eROSITA (Predehl et al. 2021) and the Square Kilometre Array (SKA; Dewdney et al. 2009) are expected to discover many new low-mass clusters missed by previous instruments, allowing us to definitely enter into the study of nonthermal phenomena in this poorly explored regime of cluster mass.

4.2. Relic, Rim, and Patch

To the best of our knowledge, the Ant Cluster is the third cluster with an SZ-derived mass $M_{500} < 2 \times 10^{14}\ M_\odot$ that hosts a radio relic (the others are A168, Dwarakanath et al. 2018; A1904, van Weeren et al. 2021). The relic is located at a considerable distance from the cluster center ($\sim$1.7 Mpc $\simeq 2r_{500}$) and shows a mildly convex morphology (Figure 1, top right panel). Relics are generally observed at 0.5–2 Mpc from the cluster center (e.g., de Gasperin et al. 2014; Nuza et al. 2017) and have a concave morphology. The mildly convex curvature of the relic in the Ant Cluster is quite atypical, and may arise from the properties of the medium encountered by the shock front during its long propagation into the cluster outskirts. Many aspects of the formation mechanisms of radio relics are still uncertain, and the discovery of more relics with similar properties will help to refine the models (e.g., Brüggen & Vazza 2020).

The classification of the Rim and Patch is still not clear. The Rim has an elongated morphology and higher surface brightness compared to the radio halo, possibly suggesting a radio relic nature. We note that this emission is projected within r_{500}, where relics should be more unlikely to observed (Vazza et al. 2012). The Patch has a very low surface brightness and potentially shows a trail of emission toward the cluster. However, the low significance of the detection makes it hard to determine the exact morphology and whether or not it is associated with some optical counterpart. Still, its peripheral location and distance to the cluster center similar to that of the relic may suggest that the Patch is also tracing a radio relic. Obviously, this hypothesis is rather speculative at the moment and deeper, multifrequency observations are required to understand its nature.

5. Conclusions

We have reported the discovery of a radio halo in PSZ2G145.92-12.53 (Ant Cluster) at $z = 0.03$ using LOFAR observations at 120–168 MHz carried out in the context of LoTSS. The halo occupies the central region of the cluster and its morphology follows that of the ICM thermal emission. Its radio power at 150 MHz of $P_{150} = (3.5 \pm 0.7) \times 10^{23}$ W Hz^{-1} and mass of $M_{500} = (1.9 \pm 0.2) \times 10^{14}\ M_\odot$ make it the least powerful and least massive system hosting a radio halo known to date. Our observations show the potential of LOFAR to detect radio halos even in low-mass systems, where the probability to form them in the context of turbulent reacceleration models is expected to be very low ($\sim$5%). Future observations of statistical samples of clusters will allow us to test the model predictions and constrain the low-power and low-mass end of the P_{150}–M_{500} relation.

We thank the anonymous referee for constructive comments that helped improve the manuscript. A.Bot. and R.J.v.W. acknowledge support from the VIDI research program with project number 639.042.729, which is financed by the Netherlands Organisation for Scientific Research (NWO). R.C., G.B., F.G., and M.R. acknowledge support from INAF mainstream project "Galaxy Clusters Science with LOFAR" 1.05.01.86.05. A.Bon. and D.N.H. acknowledge support from ERC-Stg DRANOEL 714245. V.C. acknowledges support from the Alexander von Humboldt Foundation. LOFAR (van Haarlem et al. 2013) is the LOw Frequency ARray designed and constructed by ASTRON. It has observing, data processing, and data storage facilities in several countries, which are owned by various parties (each with their own funding sources), and are collectively operated by the ILT foundation under a joint scientific policy. The ILT resources have benefited from the following recent major funding sources: CNRS-INSU, Observatoire de Paris and Université d'Orléans, France; BMBF, MIWF-NRW, MPG, Germany; Science Foundation Ireland (SFI), Department of Business, Enterprise and Innovation (DBEI), Ireland; NWO, The Netherlands; The Science and Technology Facilities Council, UK; Ministry of Science and Higher Education, Poland; Istituto Nazionale di Astrofisica (INAF), Italy. This research made use of the University of Hertfordshire high-performance computing facility and the LOFAR-UK computing facility located at the University of Hertfordshire and supported by STFC [ST/P000096/1]. This research made use of APLpy, an open-source plotting package for Python (Robitaille & Bressert 2012).

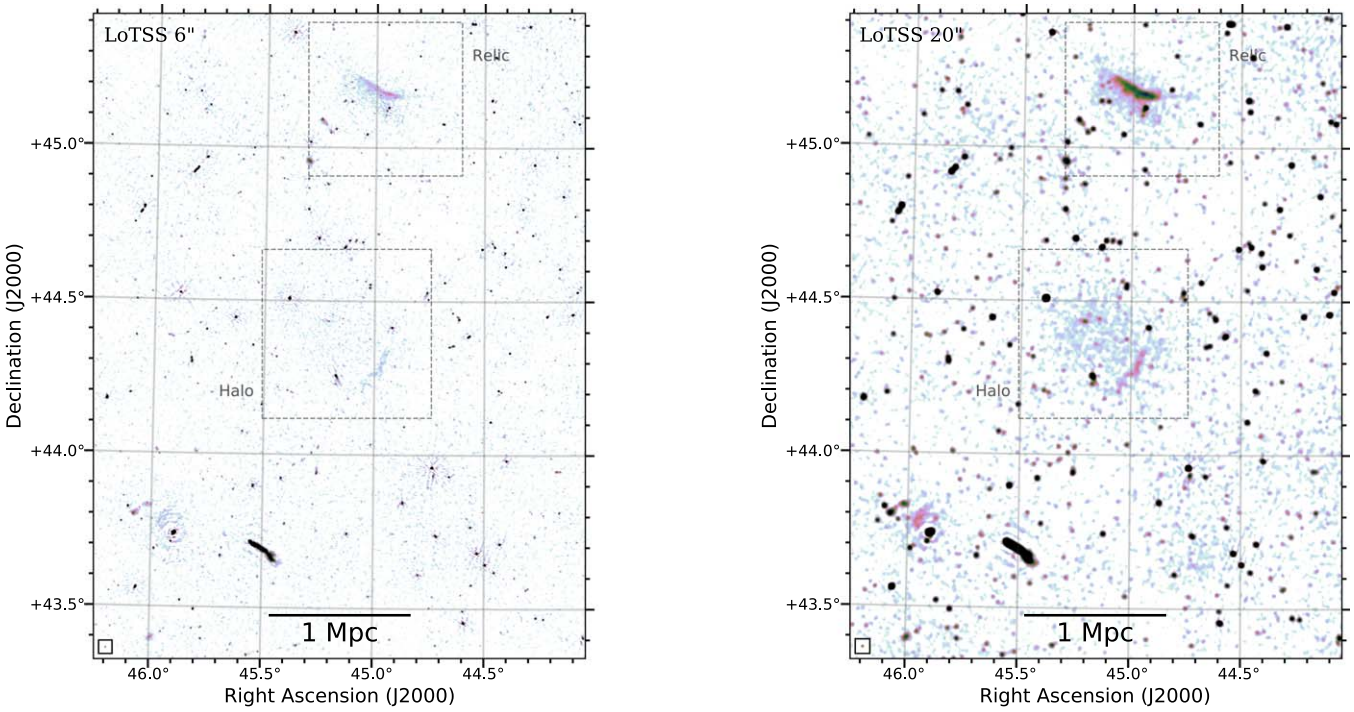

Figure 5. LoTSS images at 6″ (left) and 20″ (right) resolution and with a noise of 93 and 160 μJy beam^{-1}, respectively. The FoV and dashed boxes are the same as in the left panel of Figure 1.

Facilities: LOFAR, XMM-Newton, ROSAT.

Appendix
Images from LoTSS

In Figure 5 we show the corresponding LoTSS images at 6″ and 20″ resolution of the FoV covered by the left panel of Figure 1 as produced by the LOFAR Surveys Key Science Project team by running `ddf-pipeline` on the pointing P044+44. These images were obtained employing the third-generation calibration and imaging algorithm described in Tasse et al. (2021). Thanks to the "extraction and recalibration" method described in Section 2.1, we are able to improve the calibration toward specific targets, perform fast and flexible reimaging of the regions of interest, model and subtract discrete sources more carefully, and deeply deconvolve faint diffuse emission (see van Weeren et al. 2021 for more details).

ORCID iDs

A. Botteon https://orcid.org/0000-0002-9325-1567
R. Cassano https://orcid.org/0000-0003-4046-0637
R. J. van Weeren https://orcid.org/0000-0002-0587-1660
T. W. Shimwell https://orcid.org/0000-0001-5648-9069
A. Bonafede https://orcid.org/0000-0002-5068-4581
M. Brüggen https://orcid.org/0000-0002-3369-7735
G. Brunetti https://orcid.org/0000-0003-4195-8613
V. Cuciti https://orcid.org/0000-0003-4454-132X
D. Dallacasa https://orcid.org/0000-0003-1246-6492
F. de Gasperin https://orcid.org/0000-0003-4439-2627
G. Di Gennaro https://orcid.org/0000-0002-8648-8507
F. Gastaldello https://orcid.org/0000-0002-9112-0184
D. N. Hoang https://orcid.org/0000-0002-8286-646X
M. Rossetti https://orcid.org/0000-0002-9775-732X
H. J. A. Röttgering https://orcid.org/0000-0001-8887-2257

References

Bernardi, G., Venturi, T., Cassano, R., et al. 2016, MNRAS, 456, 1259
Botteon, A., Cassano, R., Eckert, D., et al. 2019, A&A, 630, A77
Botteon, A., Giacintucci, S., Gastaldello, F., et al. 2021, A&A, 649, A37
Boxelaar, J. M., van Weeren, R. J., & Botteon, A. 2021, A&C, 35, 100464
Brüggen, M., & Vazza, F. 2020, MNRAS, 493, 2306
Brunetti, G., & Jones, T. W. 2014, IJMPD, 23, 30007
Cassano, R., Botteon, A., Di Gennaro, G., et al. 2019, ApJL, 881, L18
Cassano, R., & Brunetti, G. 2005, MNRAS, 357, 1313
Cassano, R., Brunetti, G., Röttgering, H. J., & Brüggen, M. 2010, A&A, 509, A68
Cassano, R., Brunetti, G., & Setti, G. 2006, MNRAS, 369, 1577
Cassano, R., Ettori, S., Brunetti, G., et al. 2013, ApJ, 777, 141
Condon, J., Cotton, W., Greisen, E., et al. 1998, AJ, 115, 1693
Cuciti, V., Cassano, R., Brunetti, G., et al. 2015, A&A, 580, A97
Cuciti, V., Cassano, R., Brunetti, G., et al. 2021a, A&A, 647, A50
Cuciti, V., Cassano, R., Brunetti, G., et al. 2021b, A&A, 647, A51
de Gasperin, F., Dijkema, T. J., Drabent, A., et al. 2019, A&A, 622, A5
de Gasperin, F., van Weeren, R. J., Brüggen, M., et al. 2014, MNRAS, 444, 3130
Dewdney, P., Hall, P., Schilizzi, R., & Lazio, T. J. W. 2009, IEEEP, 97, 1482
Di Gennaro, G., van Weeren, R. J., Brunetti, G., et al. 2021, NatAs, 5, 268
Duchesne, S. W., Johnston-Hollitt, M., Offringa, A. R., et al. 2021, PASA, 38, e010
Dwarakanath, K., Parekh, V., Kale, R., & George, L. 2018, MNRAS, 477, 957
Ebeling, H., Mullis, C., & Tully, R. 2002, ApJ, 580, 774
Feretti, L., Giovannini, G., Govoni, F., & Murgia, M. 2012, A&ARv, 20, 54
Ficarra, A., Grueff, G., & Tomassetti, G. 1985, A&AS, 59, 255
Giacintucci, S., Venturi, T., Brunetti, G., et al. 2005, A&A, 440, 867
Giovannini, G., Bonafede, A., Feretti, L., et al. 2009, A&A, 507, 1257
Govoni, F., & Feretti, L. 2004, IJMPD, 13, 1549
Hardcastle, M. J., Shimwell, T. W., Tasse, C., et al. 2021, A&A, 648, A10
Hlavacek-Larrondo, J., Gendron-Marsolais, M.-L., Fecteau-Beaucage, D., et al. 2018, MNRAS, 475, 2743
Hoang, D. N., Shimwell, T. W., Osinga, E., et al. 2021, MNRAS, 501, 576
Hoang, D. N., Shimwell, T. W., van Weeren, R. J., et al. 2019, A&A, 622, A21
Kale, R., Venturi, T., Giacintucci, S., et al. 2013, A&A, 557, A99
Kale, R., Venturi, T., Giacintucci, S., et al. 2015, A&A, 579, A92
Murgia, M., Govoni, F., Markevitch, M., et al. 2009, A&A, 499, 679
Nuza, S., Gelszinnis, J., Hoeft, M., & Yepes, G. 2017, MNRAS, 470, 240

Offringa, A. R., McKinley, B., Hurley-Walker, N., et al. 2014, MNRAS, 444, 606
Osinga, E., van Weeren, R. J., Boxelaar, J. M., et al. 2021, A&A, 648, A11
Piffaretti, R., Arnaud, M., Pratt, G., Pointecouteau, E., & Melin, J.-B. 2011, A&A, 534, A109
Planck Collaboration, Ade, P. A. R., Aghanim, N., et al. 2014, A&A, 571, A29
Planck Collaboration, Ade, P. A. R., Aghanim, N., et al. 2016, A&A, 594, A27
Predehl, P., Andritschke, R., Arefiev, V., et al. 2021, A&A, 647, A1
Robitaille, T., & Bressert, E. 2012, APLpy: Astronomical Plotting Library in Python, Astrophysics Source Code Library, ascl:1208.017
Rudnick, L., & Lemmerman, J. 2009, ApJ, 697, 1341
Sarazin, C. L. 2002, in Merging Processes in Galaxy Clusters, Astrophysics and Space Science Library, Vol. 272, ed. L. Feretti, I. Gioia, & G. Giovannini (Dordrecht: Kluwer), 1
Shimwell, T. W., Röttgering, H. J., Best, P. N., et al. 2017, A&A, 598, A104
Shimwell, T. W., Tasse, C., Hardcastle, M. J., et al. 2019, A&A, 622, A1
Tasse, C., Shimwell, T. W., Hardcastle, M. J., et al. 2021, A&A, 648, A1
van Haarlem, M., Wise, M. W., Gunst, A., et al. 2013, A&A, 556, A2
van Weeren, R. J., de Gasperin, F., Akamatsu, H., et al. 2019, SSRv, 215, 16
van Weeren, R. J., Shimwell, T. W., Botteon, A., et al. 2021, A&A, in press (doi:10.1051/0004-6361/202039826)
van Weeren, R. J., Williams, W. L., Hardcastle, M. J., et al. 2016, ApJS, 223, 2
Vazza, F., Brüggen, M., van Weeren, R. J., et al. 2012, MNRAS, 421, 1868
Venturi, T., Bardelli, S., Dallacasa, D., et al. 2003, A&A, 402, 913
Venturi, T., Bardelli, S., Morganti, R., & Hunstead, R. W. 2000, MNRAS, 314, 594
Venturi, T., Giacintucci, S., Brunetti, G., et al. 2007, A&A, 463, 937
Voges, W., Aschenbach, B., Boller, T., et al. 1999, A&A, 349, 389